Doping Effects on the Ductility of a Lightweight Refractory High Entropy Alloy: Grain Boundary and Bulk Lattice Aspects

Saro San[1,2*], Yi Wang[1,2], Michael Widom[3], Yong-Jie Hu[4], David E. Alman[1], Michael C. Gao[1*]

1. National Energy Technology Laboratory, 1450 Queen Ave SW, Albany, OR 97321.
2. NETL Support Contractor, 1450 Queen Ave SW, Albany, OR 97321.
3. Department of Physics, Carnegie Mellon University, Pittsburgh, PA 15213.
4. Department of Materials Science and Engineering, Drexel University, Philadelphia, PA19104.

∗ Corresponding authors. E-mail addresses: saro.san@netl.doe.gov, michael.gao@netl.doe.gov

Abstract

Doping elements in small amounts often segregate to grain boundaries (GBs) in alloys and can significantly impact mechanical properties and performance. Refractory high-entropy alloys (RHEAs) are known for their poor ductility, especially at low temperatures. Promoting GB cohesion through segregation can be an effective approach to mitigate embrittlement. In this study, first-principles density functional theory (DFT) calculations were performed to examine the effects of important interstitial dopants (O, B, C, and N) and substitutional dopants (Cr, Y, La, and Ce) on the Σ5(310) [001] tilt GB of a lightweight RHEA $Nb_{32.5}Ti_{27.5}Mo_{22.5}Ta_{12.5}Hf_{2.5}Zr_{2.5}$. The DFT calculations reveal that certain dopants, such as B, C, Cr, N, and Y, exhibit favorable GB strengthening effects by improving bonding interactions with the bulk alloy. The impact of doping on the ductility parameter of the bulk lattice, defined as the ratio of surface energy to unstable stacking fault energy for the {110} <111> slip system, was also studied; and the results show that

doping reduces the intrinsic ductility of the alloy, decreasing the D-parameter from 2.90 to 2.55, depending on the specific dopant. The present findings provide a foundational understanding at atomic level of the effect of representative dopants on mechanical properties of RHEAs and can be used to guide future alloy design for improved mechanical properties.

Keywords: Grain boundary segregation, embrittlement, ductility, first principles calculation, deformation charge density, interstitial and substitutional doping

Introduction

The design of HEAs involves selecting elements with different atomic sizes, electronic configurations, and atomic bonding characteristics to form a highly disordered solid solution with enhanced properties [1-7]. Refractory high entropy alloys (RHEAs) primarily consist of main elements from Group IV-VI in the periodic table [8, 9]. One of the significant challenges in HEAs is how to quantify the impact of grain boundaries (GBs) on the mechanical, functional, and thermal properties of the alloy [10]. Grain boundaries, which form as a result of defects such as dislocations and vacancies, act as the sites that often localize deformation processes and can promote fracture in materials. GBs represent regions of disrupted atomic arrangements that influence mechanical behaviors, including embrittlement and plasticity [11-13]. For example, GB-induced embrittlement and reduced thermal stability have been observed in Cantor alloys, as evidenced by nanoclustering of principal elements at GBs and their detrimental effects on cohesion and mechanical properties at intermediate temperatures [14, 15]. Therefore, improving grain boundary properties is crucial for enhancing the overall performance of HEAs [16-19].

Cohesion at GBs is a critical aspect influencing the ductility of structural materials. Doping elements tend to interact with GBs, which can influence the ductility of HEAs. This interaction can contribute to energy minimization within the system [20]. Several experimental and theoretical studies demonstrated that segregation of certain dopants at GBs impact the ductility of the HEAs. Wang et al. [16] showed that oxygen-induced GB embrittlement resulting from the weak electronic interaction between oxygen (O) and the host transitional metals, leads to intergranular cracking in NbMoTaW RHEA. While elements like O have a negative impact, the addition of elements that form strong electronic bonds with the host metals, such as boron (B) and carbon (C), enhance GB cohesion and improve ductility [21-23]. This was demonstrated by Soel et al. where doping with B improved GB cohesive strength and decreased capillary-driven grain coarsening in the face-centered cubic (fcc) $Fe_{40}Mn_{40}Cr_{10}Co_{10}$ HE which resulted in a doubling of yield strength and an increase in ultimate tensile strength by 40% while maintaining or improving ductility [21].

The goal of this work is to identify doping elements that can enhance GB cohesion and intrinsic ductility of the bulk lattice and hence improve the ductility of a lightweight RHEA $Nb_{32.5}Ti_{27.5}Mo_{22.5}Ta_{12.5}Hf_{2.5}Zr_{2.5}$ (composition in atomic percentage). The aim is to provide a thorough investigation of the impact of interstitial and substitutional dopants on the Σ5 (310) [001] GB tilt structure in the RHEA in relation to ductility. This specific alloy composition was designed to have a density below 9.0 g/cm^3, and combination of acceptable ductility and fracture toughness at room temperature as well as high strength and creep resistance at elevated temperatures (>1300 °C). Interstitial dopant elements studied include C, O, B, and nitrogen (N). Substitutional doping elements studied include reactive elements that often segregate to GB, such as Ce, La, Y, and Cr. These elements have very different atomic sizes from Nb, Mo, or Ti. In addition, these reactive

elements serve as O scavengers by forming oxides that can strengthen the alloy by pin dislocation motion. The effect of dopants was simulated for the properties below, using first principles density functional theory (DFT) approach by calculating energy changes from doping and examining the atomic and electronic structures:

- GB segregation energy [24, 25]. Three sites were chosen to represent various local environments in the RHEA.
- GB strengthening energy [26, 27]. The strength is related to the resistance to deformation provided by grain boundaries and act as barriers to dislocation motion [28].
- Intrinsic ductility [29]. The impact on the bulk alloy ductility was assessed by calculating the change in intrinsic ductility parameter defined as the ratio of surface energy to unstable stacking fault energy for the {110} <111> slip system.

Computational Methods

The DFT calculations were conducted using the Vienna Ab initio Simulation Package (VASP) [30, 31]. The Projector-Augmented Wave Perdew-Burke-Ernzerhof (PAW-PBE) potentials were employed to optimize the structures [32]. The bulk lattice underwent complete relaxation with a plane wave energy cutoff set at 400 eV. Convergence tolerances of 10^{-6} eV and 10^{-4} eV/Å were implemented for electronic and ionic relaxations, respectively. The Monkhorst-Pack scheme was applied to sample the Brillouin zone, employing a k-points interval along each reciprocal lattice vector of 0.03π $Å^{-1}$. A first-order Methfessel-Paxton approach was utilized to smooth the eigenstates using an energy width of 0.2 eV.

Grain Boundary Supercell

A tilt grain boundary (GB) of Σ5(310) [001] was constructed based on the coincidence site lattice (CSL) model using the PyMatGen package [33]. A large 240-atom supercell model of $Nb_{32.5}Ti_{27.5}Mo_{22.5}Ta_{12.5}Hf_{2.5}Zr_{2.5}$ was then generated using the special quasi-random structure (SQS) provided by the Alloy Theoretic Automated Toolkit (ATAT) [34], as illustrated in **Figure 1a**. It is important to note that the minimum distance between periodic boundaries measures approximately 25 Å, while an average distance of 40 Å is required to minimize the interaction between the grains [35, 36].

GB segregation energy (E_{seg}) was calculated to assess the propensity for GB segregation [24, 25]., by determining the difference between the total energy of the GB model with and without the presence of atoms X (E_{GB}^{X} and E_{GB}, respectively) and the total energy of the bulk model with and without the atoms X (E_{bulk}^{X} and E_{bulk}). The E_{seg} was obtained using Eq. (1). The strengthening energy was also calculated to evaluate the binding strengths of the GB model with interstitial and substitutional doping [26, 27]. The strengthening energy was calculated using Eq. (2).

$$E_{seg} = (E_{GB}^{X} - E_{GB}) - (E_{bulk}^{X} - E_{bulk}) \quad (1)$$

$$\Delta E_{SE} = (E_{GB}^{X} - E_{GB}) - (E_{FS}^{X} - E_{FS}) \quad (2)$$

Here, E_{FS}^{X} and E_{FS} represents the total energy associated with the free surface of the fractured GB model as illustrated in **Figure 1(b)**, accounting for the presence or absence of adopted atoms X, respectively.

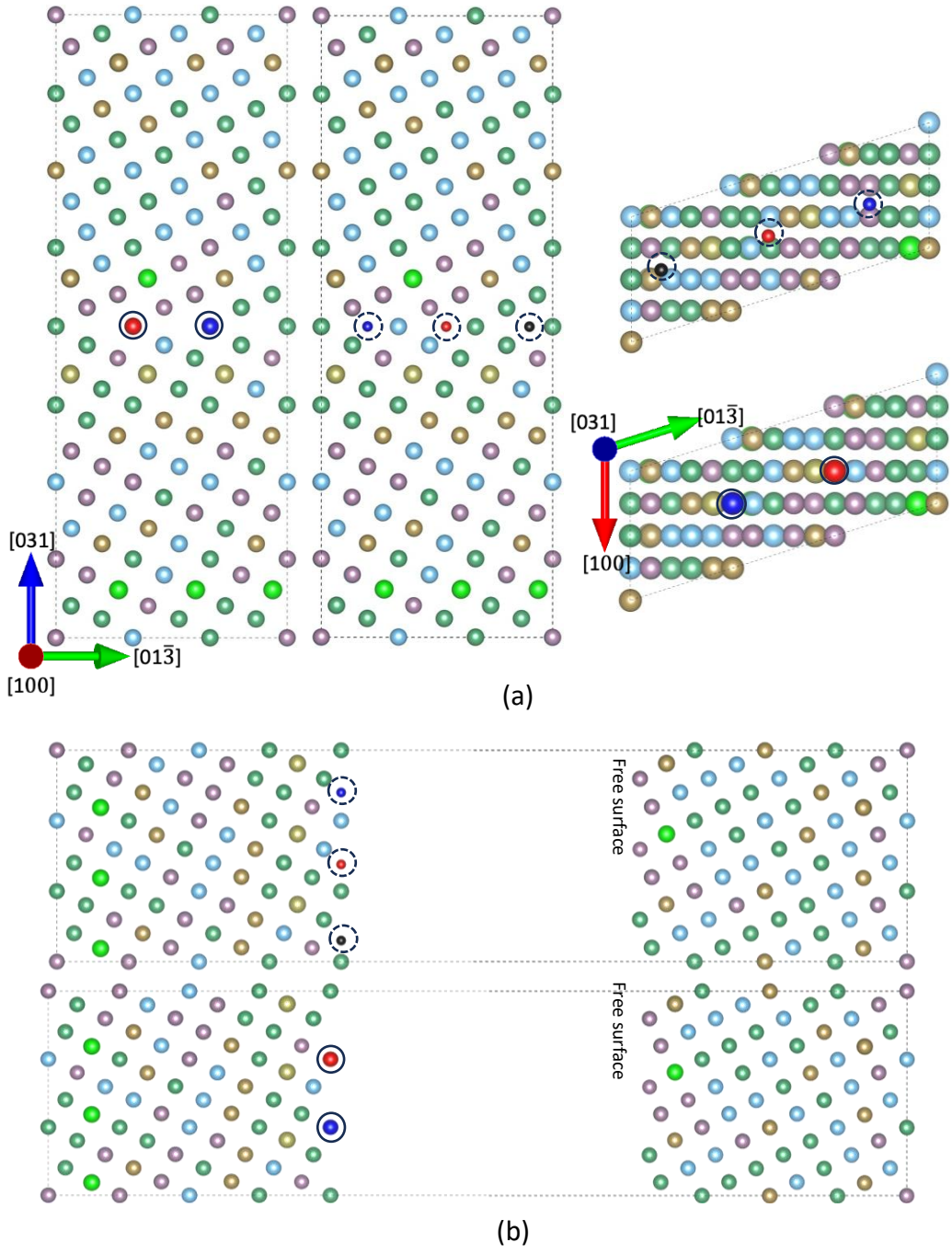

Fig. 1. Schematic illustration of the Σ5(310) grain boundary with interstitial and substitutional doping: (a) The GB in both (310) and (100) planes, while (b) the Σ5(310) free surface of the $Nb_{32.5}Ti_{27.5}Mo_{22.5}Ta_{12.5}Hf_{2.5}Zr_{2.5}$ RHEA structure used for segregation energy and strengthening energy calculations. Substitutional doping is indicated by red and blue atoms encircled with solid lines, while interstitial doping is represented by smaller red, blue, and black atoms encircled with dashed lines at the grain boundary sites.

Intrinsic Ductility of the Bulk Lattice

To investigate the effect of doping on the intrinsic ductility of the bulk RHEA, a random solid solution of a body-centered cubic (BCC) supercell was constructed comprising of 120 atoms using SQS with $[11\bar{2}] \times 5[11\bar{0}] \times 2[111]$ lattice vectors with ten layers. The supercell was fully relaxed, including both its ionic structure and volume, to obtain the equilibrium lattice parameters. Following the relaxation of the structure, an unstable stacking fault (USF) was then generated between the $(1\bar{1}0)$ plane along the [111] direction – the most preferred slip system in the BCC system. The atoms on a plane (layer) were shifted by distorting the supercell away from 90 degrees (**Figure 2c**). The applied shifts were in both directions ($\pm\frac{1}{4}[111]$) [29]. Therefore, the USF energy γ_{usf} is estimated by averaging the USF energies calculated from all layers in both directions using Eq. (3). It should be noted that the stress along the [110] direction was allowed to release while the supercell along the plane parallel to the slip plane remained fixed.

$$\gamma_{usf} = \frac{E_{USF} - E_{bulk}}{A} \tag{3}$$

where E_{USF} and E_{bulk} are the total energy of the supercell with and without an USF respectively, and A is the area of the fault plane. A vacuum layer of 10 Å was inserted in the $[1\bar{1}0]$ direction between the $(1\bar{1}0)$ planes to calculate their corresponding surface energies, as shown in **Figure 2b**. The atoms were only allowed to relax on the surface of two adjacent planes in the $(1\bar{1}0)$ plane. The surface energy is obtained for every layer in the supercell, and the resultant surface energy is the average derived from all ten calculations. The surface energy is calculated by the following equation:

$$\gamma_{sur} = \frac{E_{sur} - E_{bulk}}{2A} \tag{4}$$

where E_{sur} is the energy of the supercell with vacuum slab, A is the area of the fracture surface, and factor 2 is to count for two surfaces.

Finally, the D parameter [37-39], which is used to represent the intrinsic ductility of a material, is calculated using:

$$D = \frac{\gamma_{sur}}{\gamma_{usf}} \tag{5}$$

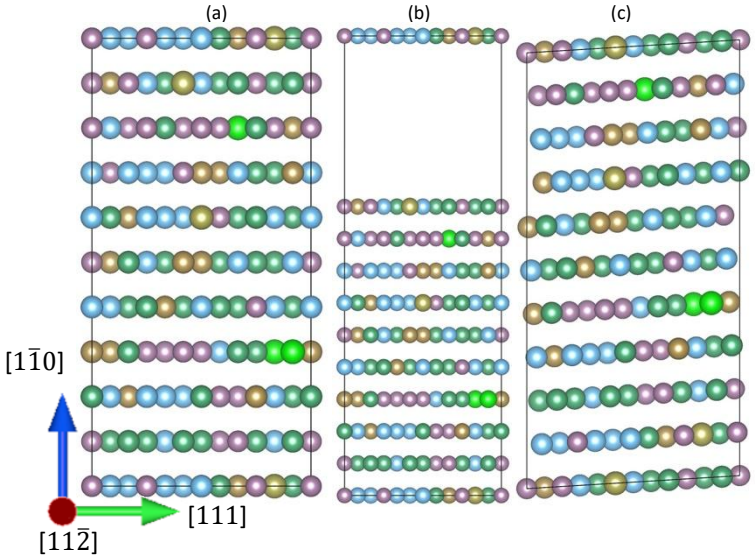

Fig. 2. The supercell structure of (a) bulk, (b) 10 Å vacuum slab to calculate surface energy, and (c) staking fault to calculate unstable stacking fault energy of RHEA $Nb_{32.5}Ti_{27.5}Mo_{22.5}Ta_{12.5}Hf_{2.5}Zr_{2.5}$.

Results

Grain Boundary with Dopants

The segregation energies of different interstitial dopants at pure Nb grain boundary are shown in **Figure 3a**. In general, a negative value indicates that dopant elements will segregate to the GB. The results show that it is energetically favorable for O, N, C, and B to segregate to the grain

boundaries of pure Nb. Specifically, B exhibits the most substantial segregation tendency with an energy of -2.48 eV, followed by -1.37 eV for C, -0.47 eV for N, and -0.22 eV for O.

Figure 3b and 3**c** illustrate the segregation energy and strengthening energy of the eight dopants at different GB sites in RHEA $Nb_{32.5}Ti_{27.5}Mo_{22.5}Ta_{12.5}Hf_{2.5}Zr_{2.5}$. Several sites were chosen for adding interstitial doping, however, we report only three at the GB; this is due to the similarity of the results. Similarly, two substitutional sites were also selected at the GB located as shown in **Figure 1a**. **Figure 3b** shows the segregation energy of each site and their average in the GB supercell of the RHEA. B, Y, C, La, and Ce demonstrate a negative segregation energy, while O, Cr, and N display a small positive segregation energy in the RHEA. Moreover, B and Y show more negative segregation energy than C, La, and Ce, indicating a higher likelihood of B and Y segregation at the GB. The predicted segregation tendency of B and C in $Nb_{32.5}Ti_{27.5}Mo_{22.5}Ta_{12.5}Hf_{2.5}Zr_{2.5}$ is consistent with the previous DFT study of an equiatomic MoNbTaW [16] and experimental measurement on pure Mo [40], which showed that both B and C tend to segregate at the GB. In contrast, Wang et al. [16] also showed that O tends to segregate at GB of MoNbTaW.

The presence of B or other dopants with very negative segregation energy can prevent O segregation. This reduces the potential for O-induced weakening of GBs and the onset of crack formation at the GBs [41]. Although B and C doping site 1, marked as small red balls circled by dashed lines (see **Figure 1a** middle panel), is preferred based on the segregation energy calculations, their favorability varies based on the specific dopant element. In contrast, the substitutional dopants prefer to reside on site 2, as marked as large red ball circled by solid lines (see **Figure 1a**).

Figure 3b further expands on this by presenting the average GB strengthening energy ΔE_{SE} associated with both interstitial and substitutional doping. The strengthening energy shows that site 2 is the most preferred site for all dopants. The B, C, Cr, N, Y, and Ce dopants show negative ΔE_{SE} values, with B being the most negative and Ce being the least negative. A more negative ΔE_{SE} suggests a stronger effect on the GB strength and cohesion. Conversely, the dopants with positive values, namely O and La – with La having the highest positive value – contribute to weaker GB strength and cohesion, potentially leading to embrittlement.

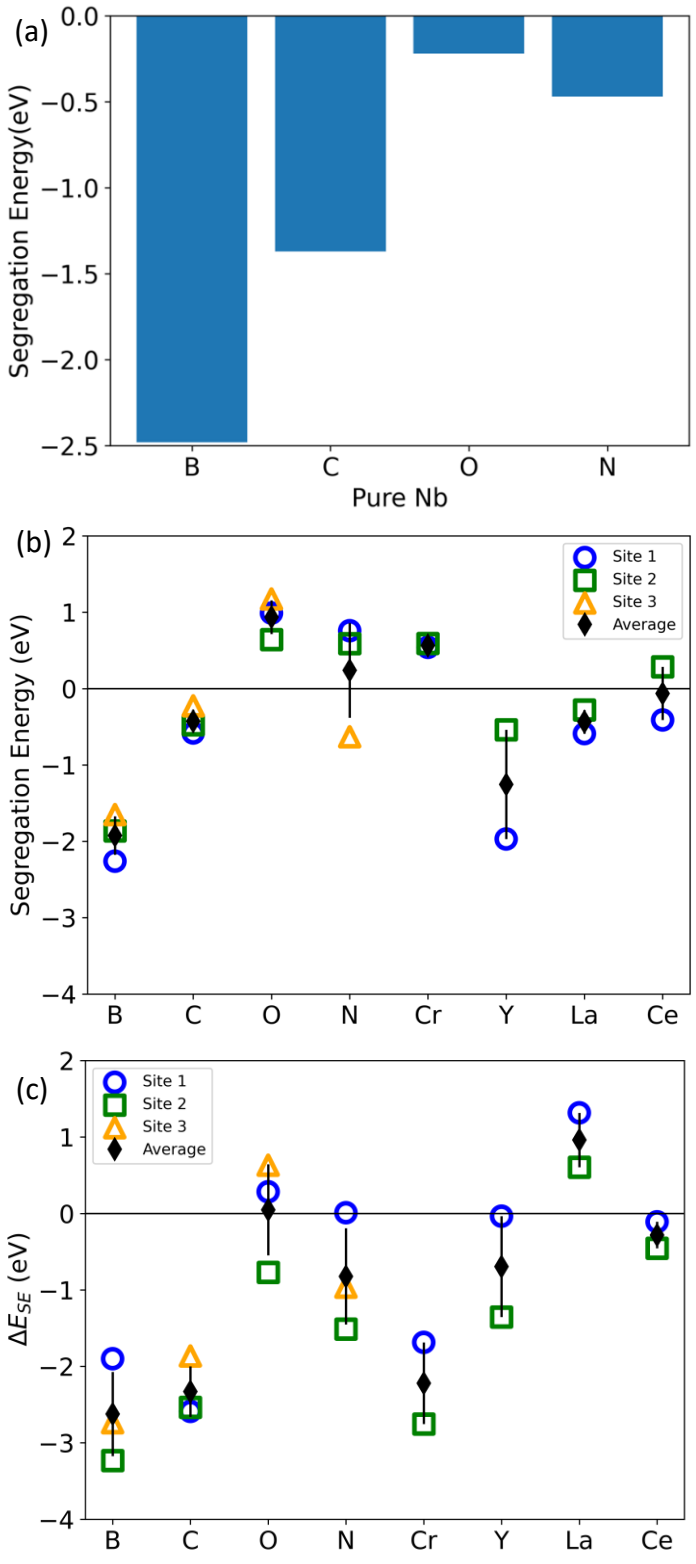

Fig. 3. Segregation energy of four interstitial doping at pure Nb grain boundary (a). Average segregation energy of doping at different sites in grain boundary (b), and average GB strengthening energy with interstitial and substitutional doping (c) in RHEA $Nb_{32.5}Ti_{27.5}Mo_{22.5}Ta_{12.5}Hf_{2.5}Zr_{2.5}$.

These results are in agreement with previous studies interrogating the impact of interstitial elements doping [16]. Negative values of strengthening energy and the segregation energy promote a more stable grain structure and enhance the boundary cohesion against the intergranular cracking [42-44]. RHEAs with high Cr contents tend to be brittle, and the cohesion effect of Cr on the GB is a structure-dependent [45]. The present study shows that Cr enhances the grain boundary cohesion. Studies on other materials systems have drawn similar conclusions [45-47].

Intrinsic Ductility

Figure 4 (a-c) shows the distribution of unstable stacking fault energy γ_{usf}, surface energy γ_{sur} and intrinsic ductility D-parameter in the RHEA, in both pristine (undoped) and doped states. Similar plots for different sites of each doping are demonstrated in **Figure S1** in Supplementary Materials. The mean values (in red triangles) were determined from the array of 20 data points each for γ_{usf}, alongside 10 data points each for surface energy and D parameter. The wide scattering of γ_{usf} indicates that γ_{usf} is very sensitive to local chemistry near the stacking fault, agreeing with a prior study [29].

Depending on the concentration, dopant elements can have a large impact on the D parameter of RHEAs by causing local atomic structural variations, promoting electron charge transfer, and reshaping the potential energy landscape of the material. In the D parameter calculations, the dopants of large atomic size were substituted for Mo, Nb or Ti at very low content of 0.775 at.%, while O, C, and N atoms occupies the octahedron interstitial sites. Calculations were made for five different sites per doping case in the bulk lattice. The results are within the uncertainty range, as shown in **Figure S2**. **Figure 4a** shows the effects of doping on the USFE. Interstitial dopants such as C, N, and O, as well as substitutional Ce, increase the USFE. In contrast, elements such as B, Cr, La, and Y exhibit no measurable influence on USFE. This increase in USFE, in turn, leads to

a reduction in the D parameter. Doping on surface energy is shown in **Fig. 4b**. **Figure 4c** compares the doping effect on the ductility from a single dopant. Ce has the most negative impact on the D parameter, followed by N, O, and C. B has a small positive impact, followed by Cr. Y has no effect. **Figure 4d** shows that the average D parameter decreases sharply with increasing interstitial doping contents. With doping two O atoms, the D parameter drops to 2.55 from 2.90. The results suggest that it is crucial to minimize oxygen content during RHEA synthesis.

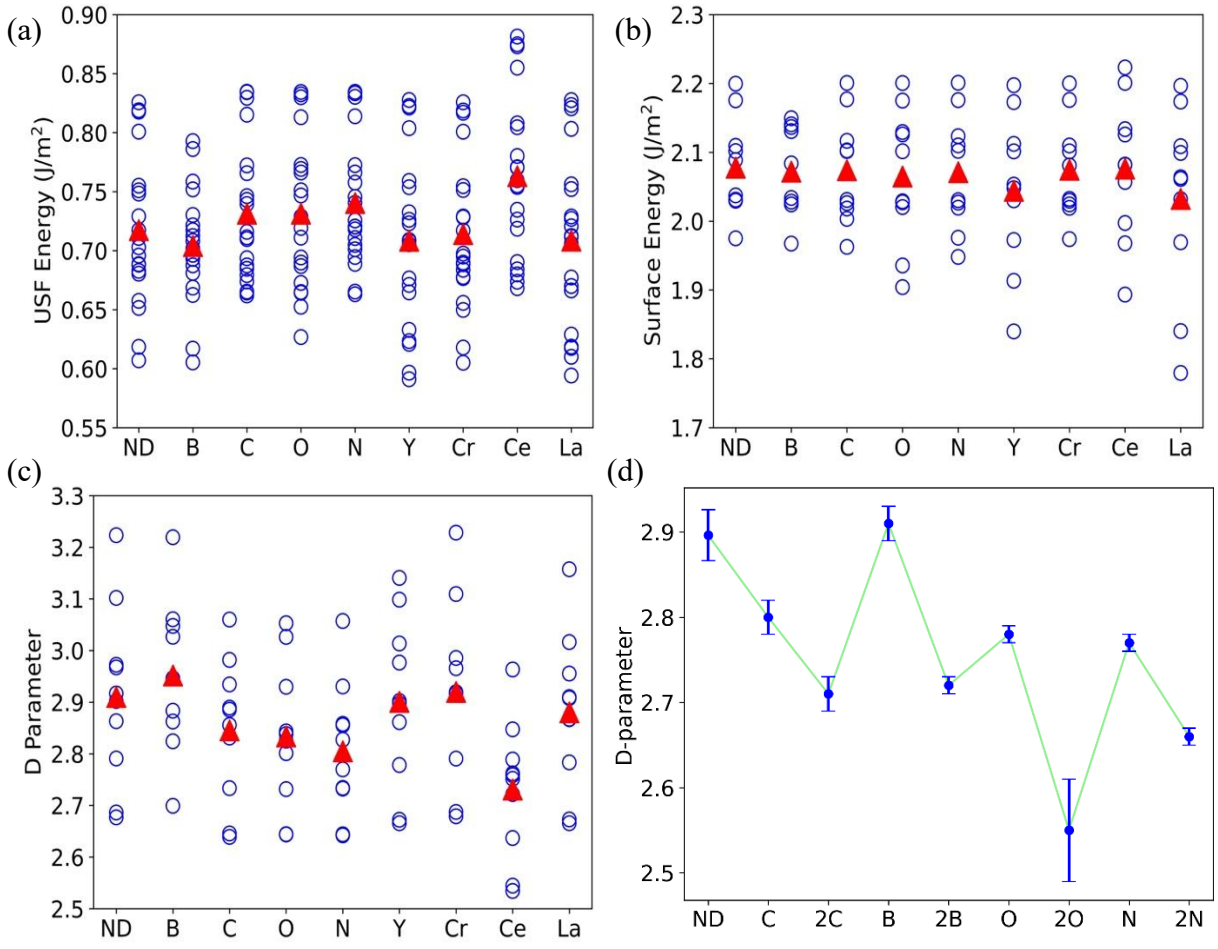

Fig. 4. The distribution of (a) unstable stacking fault energy, (b) surface energy, (c) D-parameter for a single interstitial and substitutional dopant, and (d) D-parameter with two interstitial doping atoms per supercell in RHEA $Nb_{32.5}Ti_{27.5}Mo_{22.5}Ta_{12.5}Hf_{2.5}Zr_{2.5}$. ND are calculations are for the undoped (pristine) condition. Red triangles represent mean values.

Discussion

Charge Transfer

Charge density is an essential aspect of the investigating electronic structure and provides valuable insights into the dynamics of electronic flow and their mutual interaction. Therefore, an analysis of the charge density distribution at the Σ5(310) [001] GB was calculated, and **Figure 5** compares the deformation charge density plot of the investigated RHEA along the (310) plane at GB. The deformation charges of single and double B doping in the bulk lattice are presented in **Figure S5**. In **Figure 5a**, it is shown that the incorporation of B dopant within the GB interstitial site causes an increased charge density. This results in a significant charge exchange between the B atom with its nearby transition metals, Mo, Ta, Ti, and Nb atoms, with an approximate charge density of -0.01eBohr^{-3} toward Mo and 0.01eBohe^{-3} toward Nb. However, a more significant accumulation of charge is observed between B and Nb compared to the interaction of B with other adjacent metallic elements. This rise in charge causes stronger electronic interactions between B and the metallic atoms, leading to the formation of covalent bonds and promoting stronger cohesion within the GB of the RHEA. A similar effect is observed when C dopant is introduced, with an interaction of charge with all its neighboring transition metals. However, in contrast, this phenomenon is less prominent when N (-0.005 eBohr^{-3}) and O (0.005 eBohr^{-3}) dopants are introduced. The charge accumulation between these dopants and their neighboring metallic elements within the GB interstitial site is relatively lower, resulting in a weakening of interatomic bonds. From the figures, it can be observed a clear interaction between Cr and Y with their neighboring atoms. In contrast, the electron distribution uniformly around the Ce and La transition metals without observable directionality suggests the formation of metal bonds.

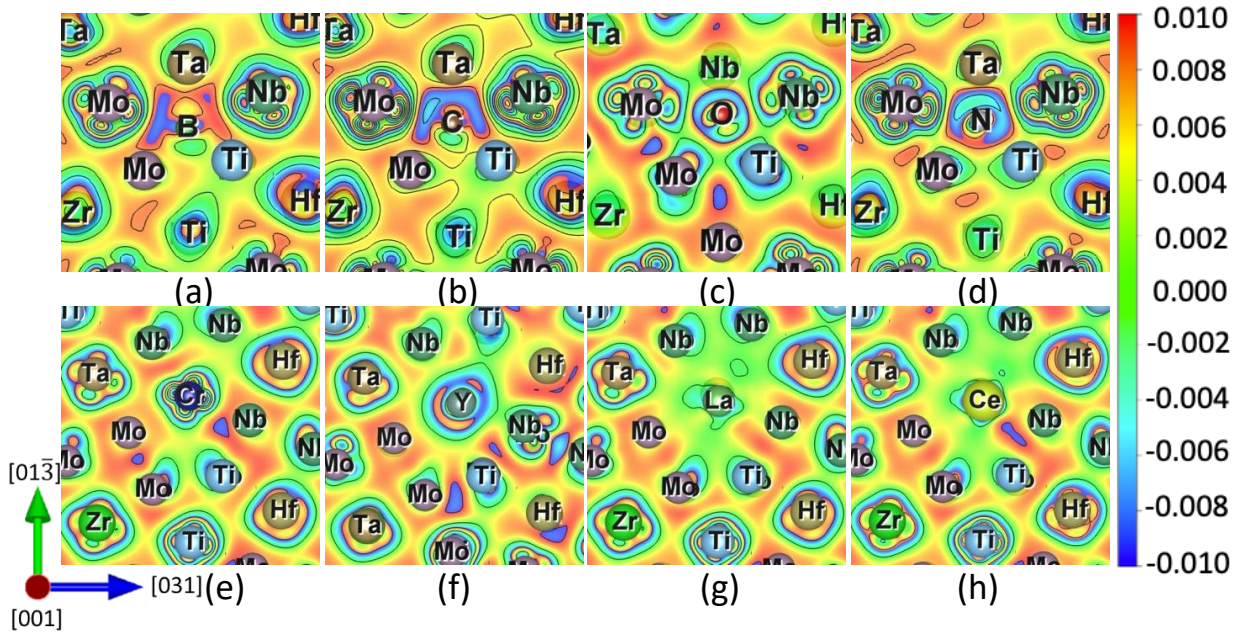

Fig. 5. Deformation charge density distributions in the unit of eBohr^{-3} Σ5(310) [001] GB in $Nb_{32.5}Ti_{27.5}Mo_{22.5}Ta_{12.5}Hf_{2.5}Zr_{2.5}$ RHEA, plotted in the plane containing interstitial elements: (a) boron, (b) carbon, (c) oxygen, and (d) nitrogen; and substitutional elements: (e) chromium, (f) yttrium, (g) lanthanum, and (h) cerium.

The density of states (DOS) for the GB supercell of $Nb_{32.5}Ti_{27.5}Mo_{22.5}Ta_{12.5}Hf_{2.5}Zr_{2.5}$ is presented in **Figure 6**. The corresponding figures for the additional dopants are presented in the Supplementary Material, **Figure S3**. The total DOS is mostly derived from the *d* orbital from each constituent element in RHEAs, while the contribution from the *s* and *p* orbitals is negligible as shown in **Figure S4**. The total density of states (TDOS) of the components in their pure environments is different; however, once these elements form the HEAs, their respective *3d, 4d,* or *5d* electrons interact with each other. The addition of dopant elements introduces new energy states, altering the electronic properties of HEAs. However, due to the type and concentration of the dopant element, the DOS does not exhibit peaks or variations at specific energy levels. For example, B (C, N, O) contributes around 3 states/eV through its *s* (*p*) orbital, which is negligible compared to the contribution from the *d* orbitals of the transition metal elements of the host alloy.

Interestingly, the analysis revealed that there is little DOS interaction resulting from the substituting dopant-induced states with the hosting element in the HEA. These observations help to explain why the chemical contribution of the *s* orbital solutes, for all the dopants, was found to be close to zero (shown in **Figure S4**). This suggests that the DOS description for the electronic interaction between the dopant and the host atoms might not play a significant role in determining the grain boundary strength.

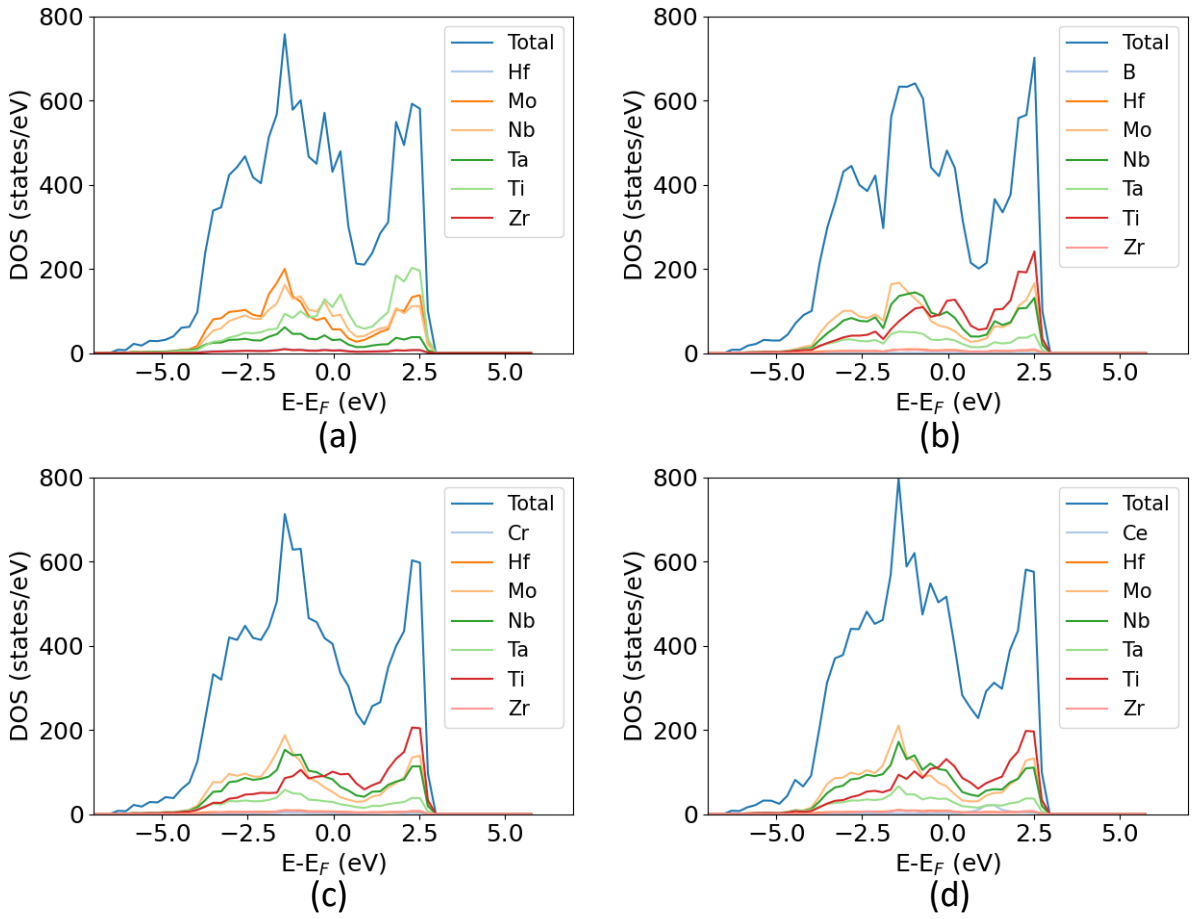

Fig. 6. Total and partial density of states of the GB supercell for the HEA with (a) no dopant, (b) B dopant, and (c) Cr, and (d) Ce in $Nb_{32.5}Ti_{27.5}Mo_{22.5}Ta_{12.5}Hf_{2.5}Zr_{2.5}$.

Intrinsic ductility and Strengthening energy

GB Strengthening Energy

Recent studies have explored the relationship between grain boundary energy and segregation phenomena in HEAs [17, 48-50]. These studies have particularly focused on how grain boundary energy affects segregation at the boundaries in equiatomic FeMnNiCoCr HEAs, providing insights into the mechanisms governing segregation behavior at grain boundaries [17] . Experimental and theoretical investigations have shown that doping with low concentrations of additional elements can impact the properties of HEAs [51]. For instance, B can enhance grain boundary cohesion and potentially improve the ductility of RHEAs [52]. Small B additions in RHEAs tend to segregate to GBs rather than dissolve in the matrix [53]. An example is an $Al_{0.1}CrNbVMo$ RHEA doped with 0.015 at.% B: atom probe tomography confirmed B enrichment at grain boundaries with no boride precipitates forming [54]. This B-segregated RHEA showed a 15% higher compression yield strength (~2,933 MPa) and 26% greater ductility (~25.9% compression fracture strain) compared to the undoped alloy [54]. Notably, adding B changed the fracture mode from intergranular to transgranular, indicating a more robust grain boundary cohesion [54]. These improvements are attributed to B segregating at GBs which strengthens the boundaries without sacrificing ductility [53, 54]. A recent study on $Hf_xMo_{0.5}NbTa_xTiV_{1.5-x}Zr_x$ RHEAs further demonstrated that B doping significantly improves grain boundary strength, increasing hardness from 5.0 to 6.0–6.2 GPa and enhancing plastic strain from 9% to 27–37% [55]. Additionally, the alloys maintained their strength at high temperatures, making them promising for applications requiring both toughness and softening resistance [55].

Moreover, the introduction of C into the alloy system has been shown to enhance strength and refine the grain structure, thereby influencing both the yield strength and ductility of the material [16, 56-59]. For example, a study by Wang et al. [16] show doping up to 0.15 at% C causes C to preferentially segregate at the GBs, effectively displacing embrittling O impurities from those sites. This substitution of O by C strengthens the boundaries and eliminates intergranular micro-cracks in the as-cast alloy [16]. However, when the C content exceeds ~0.15 at%, it no longer stays in a solid solution but instead forms carbide precipitates along GBs. Such carbide formation at the boundaries was observed at higher doping (e.g. 0.5 at.% C) and was correlated with a decline in mechanical properties [16]. This suggests the importance of keeping C content low to promote GB segregation without triggering second-phase (carbide) formation.

Our results indicate that O tends not to segregate at the grain boundary of RHEA $Nb_{32.5}Ti_{27.5}Mo_{22.5}Ta_{12.5}Hf_{2.5}Zr_{2.5}$, contrasting its weak segregation at GB of pure Nb with a segregation energy of -0.22 eV. Oxygen segregation at GB contributes to the weakening of the grain boundary cohesion due to its positive strengthening energy and causes embrittlement, for example, promoting intergranular fracture. Our DFT results align with the concept of strengthening energy as demonstrated by Wang et al. [16] , although their study suggests that O segregates at the grain boundary of NbMoTaW RHEA. It is not surprising to see oxygen segregation behavior may depend on the alloy composition. Interstitial O atoms can also enhance lattice distortion, thereby impeding dislocation movement and contributing to solid solution strengthening. This effect was observed in a TiZrNb medium-entropy alloy, where doping with up to 6 at.% O increased the room-temperature compressive yield strength from 670 MPa to 1300 MPa, while maintaining a compressive strain over 50% across all temperatures [60]. However, the interaction of O with GB

can also lead to embrittlement. In nickel-based superalloys like alloy 718, oxygen diffusion into stressed grain boundaries ahead of a crack tip can cause decohesion, resulting in quasi-brittle intergranular fracture [61]. Furthermore, our DFT calculations show that oxygen doping in trace amounts to the bulk noticeably decreases the D parameter – the intrinsic ductility.

Our study also reveals a clear tendency to segregate at GB for dopants such as Y, La, C, and Ce and unfavorable segregation for dopants such as O, Cr, and N in the RHEA (see **Fig. 5b**). Our findings on La's and Ce's segregation is noteworthy, providing theoretical insights into La's and Ce's role of grain boundary segregation behavior in RHEAs observed by Yao et al. [62] and Xu et al. [63]. Yao et al. found Ce strongly segregates to grain boundaries, causing pronounced grain refinement at the lowest addition (0.005% Ce). With 0.005% Ce, the alloy had a fine equiaxed grain structure and achieved a high yield strength (~964 MPa) while retaining good ductility (~7.15% elongation). The improved strength is attributed in part to grain-boundary strengthening from the refined grains, and Ce segregation likely enhanced the interface cohesion. Increasing Ce to 0.01% led to even more Ce at the boundaries (~1.17 at% at GBs) and triggered the formation of a brittle ω-like phase along grain boundaries, dramatically reduced ductility. Xu et al. [63] found that 0.5 at.% La significantly reduced grain size and increased strength of $NbMoTiVSi_{0.2}$ due to grain refinement, but also promoted the formation of brittle intermetallic, reducing ductility. In contrast, our results with 0.4 at.% La shows a tendency of grain boundary segregation but no significant GB strengthening effect. In summary, to improve the ductility of RHEAs through GB doping, it is very important to keep the dopant content low so that no brittle compounds can form at GB.

Intrinsic Ductility and Lattice Distortion

While this work primarily focuses on the GB segregation behavior of doping and its impact on mechanical properties of the RHEA, dopants can favor dissolved in the BCC solid solution matrix, segregation at GB, or partition between GB and matrix, depending on the individual dopant and its content. Therefore, studying the intrinsic ductility of the BCC phase upon doping provides a comprehensive understanding of the doping effect. Our theoretical study predicts a noticeable reduction in the D parameter upon doping C, O, N, and Ce. In agreement with another DFT work by Sundar et al. [64], doping Cr does not decrease the D parameter, which is counterintuitive to experimental observation. This suggests that the D parameter does not work well for all alloys. Hu et al. studied lattice distortion (LD) that emerges as a major contributor to strength, yet it must be accompanied by favorable electronic and thermodynamic conditions to preserve a ductile single-phase structure [65], which is found to depend primarily on valence electron concentration (VEC) and d-band filling. LD is minimized around VEC 5.5 e/atom, where the d-band is half-filled. As the VEC moves away from this value, LD increases, causing atoms to shift more in the structure. Compositions with large-size atoms or electronic mismatch tend to suffer a strong drive for phase separation in low-entropy systems. Therefore, RHEAs with multiple principal elements leverage high configurational entropy to stabilize a single, highly distorted lattice [65]. However, RHEA with larger VEC causes the structure toward instability. As a consequence of these effects, the strength–ductility mapping of the explored compositional space shows only a weak trade-off, with a broad distribution of alloys achieving concurrent high yield strength and intrinsic ductility [65] . In particular, tuning the alloy's VEC to around 4.7 e/atom is predicted to yield the best balance between strength and ductility. Another compositional factor is doping, which changes the value of VEC of the RHEA and can influence the level of LD.

Doping may inevitably induce local lattice distortion and hence affect the strength of the bulk lattice, therefore, it is useful to analyze how the doping may impact lattice distortion in RHEA $Nb_{32.5}Ti_{27.5}Mo_{22.5}Ta_{12.5}Hf_{2.5}Zr_{2.5}$. **Figure S6** – **Figure S8** demonstrates the analytical distribution of interatomic distances within the bulk RHEA. The calculated lattice distortion for the RHEA and doped variants are listed in Table S1. Doping Cr causes a noticeable increase in lattice distortion, and hence, an increase in strength is anticipated. On the other hand, doing La and Y causes a noticeable decrease in lattice distortion. The change in lattice distortion due to other dopants is very small. This is expected since the dopant content is kept small intentionally in the present study.

Conclusion

We investigated the segregation behavior, strengthening energy, and charge transfer mechanisms at the Σ5(310) tilt grain boundary, providing a comprehensive insight into the relationship between doping, electronic structure, and ductility of $Nb_{32.5}Ti_{27.5}Mo_{22.5}Ta_{12.5}Hf_{2.5}Zr_{2.5}$. Our findings can be summarized:

1. B, C, Cr, N, and Y, exhibit favorable strengthening energies, due to their ability to enhance bonding interactions with the host material.
2. Although C doping may lead to segregation, it compromises intrinsic ductility by reducing the D-parameter. In contrast, elements such as O and La showed a tendency to weaken GB cohesion.
3. O contributed to embrittlement and reduced ductility due to its positive strengthening energy.
4. Ce segregation was found to reduce ductility by lowering the D-parameter, while La showed little influence on strengthening but segregated significantly at the GB.

5. B and C dopants induced strong charge accumulation at the GB, other elements such as N and O exhibited weaker charge interactions, which contributed to lower cohesion.
6. The DOS analysis revealed that dopant-induced electronic states interact minimally with the host's electronic environment, suggesting that the dopants' impact on GB properties primarily arises from structural rather than electronic contributions.

Future experimental studies combined with advanced theoretical modeling will be crucial to explain the underlying mechanisms further and optimize doping strategies for HEA.

Authors' contributions

The project was conceived by M. C. G. and D. E. A. The calculations and data generation were carried out by S. S. All authors actively engaged in the discussion and interpretation of the results and contributed to the writing of the manuscript. All authors thoroughly edited and proofread the final manuscript.

Data Availability Statement

All data are listed in tables or presented in figures in the main text or Supplementary Material.

Acknowledgments

This work was sponsored by the Department of Energy ARPA-E ULTIMATE program under Award Number DE-AR0002337. The authors acknowledge inspiring discussions and guidance from ARPA-e Program Directors Zhigang Zak Fang and Phil Kim. This research used resources of the National Energy Research Scientific Computing Center, a DOE Office of Science User Facility supported by the Office of Science of the U.S. Department of Energy under Contract No.

DE-AC02-05CH11231 using NERSC award ALCC-ERCAP0022624 and ALCC-ERCAP0029917.

Conflict of Interest: The authors declare there is no conflict of interest.

Supplementary Materials

Supplementary material can be found in the online version at DOI

Reference

[1] M.C. Gao, J.-W. Yeh, P.K. Liaw, Y. Zhang, High-entropy alloys: fundamentals and applications, Springer International Publishing, 2016. DOI: 10.1007/978-3-319-27013-5
[2] J.W. Yeh, S.K. Chen, S.J. Lin, J.Y. Gan, T.S. Chin, T.T. Shun, C.H. Tsau, S.Y. Chang, Nanostructured high-entropy alloys with multiple principal elements: novel alloy design concepts and outcomes, Advanced Engineering Materials **6**(5), 299-303 (2004)
[3] B. Cantor, Multicomponent high-entropy Cantor alloys, Progress in Materials Science **120**, 100754 (2020)

[4] X. Lim, Mixed-up metals make for stronger, tougher, stretchier alloys, Nature News **533**(7603), 306-306 (2016)
[5] Y.F. Ye, Q. Wang, J. Lu, C.T. Liu, Y. Yang, High-entropy alloy: challenges and prospects, Materials Today **19**(6), 349-362 (2016)
[6] B. Gludovatz, A. Hohenwarter, D. Catoor, E.H. Chang, E.P. George, R.O. Ritchie, A fracture-resistant high-entropy alloy for cryogenic applications, Science **345**(6201), 1153-1158 (2014)
[7] A. Gali, E.P. George, Tensile properties of high-and medium-entropy alloys, Intermetallics **39**, 74-78 (2013)
[8] O.N. Senkov, D.B. Miracle, K.J. Chaput, J.-P. Couzinie, Development and exploration of refractory high entropy alloys—A review, Journal of Materials Research **33**(19), 3092-3128 (2018)
[9] O.N. Senkov, G.B. Wilks, D.B. Miracle, C.P. Chuang, P.K. Liaw, Refractory high-entropy alloys, Intermetallics **18**(9), 1758-1765 (2010)
[10] D. Raabe, M. Herbig, S. Sandlöbes, Y. Li, D. Tytko, M. Kuzmina, D. Ponge, P.P. Choi, Grain boundary segregation engineering in metallic alloys: A pathway to the design of interfaces, Current Opinion in Solid State and Materials Science **18**(4), 253-261 (2014)
[11] P.R. Cantwell, M. Tang, S.J. Dillon, J. Luo, G.S. Rohrer, M.P. Harmer, Grain boundary complexions, Acta Materialia **62**, 1-48 (2014)
[12] T.J. Rupert, The role of complexions in metallic nano-grain stability and deformation, Current Opinion in Solid State and Materials Science **20**(5), 257-267 (2016)
[13] J. Hu, Y.N. Shi, X. Sauvage, G. Sha, K. Lu, Grain boundary stability governs hardening and softening in extremely fine nanograined metals, Science **355**(6331), 1292-1296 (2017)
[14] B.X. Cao, H.J. Kong, L. Fan, J.H. Luan, Z.B. Jiao, J.J. Kai, T. Yang, C.T. Liu, Heterogenous columnar-grained high-entropy alloys produce exceptional resistance to intermediate-temperature intergranular embrittlement, Scripta Materialia **194**, 113622 (2021)
[15] K. Ming, L. Li, Z. Li, X. Bi, J. Wang, Grain boundary decohesion by nanoclustering Ni and Cr separately in CrMnFeCoNi high-entropy alloys, Science Advances **5**(12), eaay0639 (2019)
[16] Z. Wang, H. Wu, Y. Wu, H. Huang, X. Zhu, Y. Zhang, H. Zhu, X. Yuan, Q. Chen, S. Wang, Solving oxygen embrittlement of refractory high-entropy alloy via grain boundary engineering, Materials Today **54**, 83-89 (2022)

[17] L. Li, R.D. Kamachali, Z. Li, Z. Zhang, Grain boundary energy effect on grain boundary segregation in an equiatomic high-entropy alloy, Physical Review Materials **4**(5), 053603 (2020)
[18] R. Wu, A.J. Freeman, G.B. Olson, First principles determination of the effects of phosphorus and boron on iron grain boundary cohesion, Science **265**(5170), 376-380 (1994)
[19] P. Sathiyamoorthi, J. Basu, S. Kashyap, K.G. Pradeep, R.S. Kottada, Thermal stability and grain boundary strengthening in ultrafine-grained CoCrFeNi high entropy alloy composite, Materials & Design **134**, 426-433 (2017)
[20] R. Kirchheim, Reducing grain boundary, dislocation line and vacancy formation energies by solute segregation. I. Theoretical background, Acta Materialia **55**(15), 5129-5138 (2007)
[21] J.B. Seol, J.W. Bae, Z. Li, J.C. Han, J.G. Kim, D. Raabe, H.S. Kim, Boron doped ultrastrong and ductile high-entropy alloys, Acta Materialia **151**, 366-376 (2018)
[22] S. Suzuki, M. Obata, K. Abiko, H. Kimura, Role of carbon in preventing the intergranular fracture in iron-phosphorus alloys, Transactions of the Iron and Steel Institute of Japan **25**(1), 62-68 (1985)
[23] S. Son, J. Lee, P. Asghari-Rad, G.H. Gu, F. Haftlang, H.S. Kim, A facile strengthening method by co-doping boron and nitrogen in CoCrFeMnNi high-entropy alloy, Materials Science and Engineering: A **846**, 143307 (2022)
[24] X. Wu, Y.-W. You, X.-S. Kong, J.-L. Chen, G.N. Luo, G.-H. Lu, C.S. Liu, Z. Wang, First-principles determination of grain boundary strengthening in tungsten: dependence on grain boundary structure and metallic radius of solute, Acta Materialia **120**, 315-326 (2016)
[25] Y.J. Hu, Y. Wang, W.Y. Wang, K.A. Darling, L.J. Kecskes, Z.K. Liu, Solute effects on the Sigma 3 (111) 1(1)over-bar0 tilt grain boundary in BCC Fe: Grain boundary segregation, stability, and embrittlement, Computational Materials Science **171**, 109271 (2020)
[26] M.A. Gibson, C.A. Schuh, A compilation of ab-initio calculations of embrittling potencies in binary metallic alloys, Data in brief **6**, 143-148 (2016)
[27] M.A. Gibson, C.A. Schuh, A survey of ab-initio calculations shows that segregation-induced grain boundary embrittlement is predicted by bond-breaking arguments, Scripta Materialia **113**, 55-58 (2016)
[28] S. Kumar, P. Pandey, K. Chattopadhyay, Influence of interfacial and strain energies on γ′ coarsening kinetics in complex concentrated alloys, Materialia **33**, 102018 (2024)

[29] Y.-J. Hu, A. Sundar, S. Ogata, L. Qi, Screening of generalized stacking fault energies, surface energies and intrinsic ductile potency of refractory multicomponent alloys, Acta Materialia **210**, 116800 (2021)
[30] G. Kresse, J. Furthmüller, Software vasp, vienna, 1999, Phys. Rev. B **54**(11), 169-169 (1996)
[31] G. Kresse, J. Furthmuller, Vienna ab-initio simulation package (VASP): The guide, VASP Group, Institut fur Materialphysik, Universitat Wien, Sensengasse **8**, (2002)
[32] J.P. Perdew, K. Burke, M. Ernzerhof, Generalized gradient approximation made simple, Physical review letters **77**(18), 3865-3865 (1996)
[33] Z. Rong, D. Kitchaev, P. Canepa, W. Huang, G. Ceder, An efficient algorithm for finding the minimum energy path for cation migration in ionic materials, The Journal of Chemical Physics **145**(7), 074112 (2016)
[34] A. Van de Walle, P. Tiwary, M. De Jong, D.L. Olmsted, M. Asta, A. Dick, D. Shin, Y. Wang, L.Q. Chen, Z.K. Liu, Efficient stochastic generation of special quasirandom structures, Calphad **42**, 13-18 (2013)
[35] F. Zhang, C. Zhang, S.L. Chen, J. Zhu, W.S. Cao, U.R. Kattner, An understanding of high entropy alloys from phase diagram calculations, Calphad **45**, 1-10 (2014)
[36] H. Zheng, X.-G. Li, R. Tran, C. Chen, M. Horton, D. Winston, K.A. Persson, S.P. Ong, Grain boundary properties of elemental metals, Acta Materialia **186**, 40-49 (2020)
[37] M.J. Mehl, D.A. Papaconstantopoulos, N. Kioussis, M. Herbranson, Tight-binding study of stacking fault energies and the Rice criterion of ductility in the fcc metals, Physical Review B **61**(7), 4894 (2000)
[38] J. Zhao, Y.C. Jiang, L. Sun, H.R. Gong, X. Gong, Effect of alloying elements on stacking fault energy and ductility of iron, Vacuum **194**, 110633 (2021)
[39] Z. Wu, W.A. Curtin, Brittle and ductile crack-tip behavior in magnesium, Acta Materialia **88**, 1-12 (2015)
[40] S. Jakob, A. Hohenwarter, A. Lorich, W. Knabl, R. Pippan, H. Clemens, V. Maier-Kiener, Assessment of grain boundary cohesion of technically pure and boron micro-doped molybdenum via meso-scale three-point-bending experiments, Materials & Design **207**, 109848 (2021)

[41] G.L. Krasko, Effect of impurities on the electronic structure of grain boundaries and intergranular cohesion in iron and tungsten, Materials Science and Engineering: A **234-236**, 1071-1074 (1997)
[42] Z. Huang, P. Wang, F. Chen, Q. Shen, L. Zhang, Understanding solute effect on grain boundary strength based on atomic size and electronic interaction, Scientific Reports **10**(1), 16856 (2020)
[43] V.I. Razumovskiy, A.Y. Lozovoi, I.M. Razumovskii, First-principles-aided design of a new Ni-base superalloy: Influence of transition metal alloying elements on grain boundary and bulk cohesion, Acta Materialia **82**, 369-377 (2015)
[44] T. Ossowski, E. Wachowicz, A. Kiejna, Effect of iron additions on intergranular cohesion in chromium, Journal of Physics: Condensed Matter **21**(48), 485002 (2009)
[45] S. Shi, L. Zhu, H. Zhang, Z. Sun, Segregation effects of Y, Ti, Cr and Si on the intergranular fracture of niobium, Journal of Alloys and Compounds **711**, 637-642 (2017)
[46] C. Liu, K. Abiko, M. Tanino, Role of chromium in the intergranular fracture of high purity Fe-P-Cr alloys with small amounts of carbon, Materials Science and Engineering: A **176**(1-2), 363-369 (1994)
[47] E. Wachowicz, T. Ossowski, A. Kiejna, Cohesive and magnetic properties of grain boundaries in bcc Fe with Cr additions, Physical Review B **81**(9), 094104 (2010)
[48] W. Zhang, L. Huang, J. Liang, Y. Li, W. Bai, B. Jiao, D. Kan, J. Li, W. Zhang, Competitive segregation to grain boundaries between Cr and Co in FeNiCrCo alloy, Surface and Interface Analysis **56**(8), 515-524 (2024)
[49] L. Yan, G. Li, X. Liang, H. Peng, Fine-Grained FeCoNi(CuAl)x High Entropy Alloys: Phase Transformation, Microstructure Evolution and Mechanical Properties, Frontiers in Materials **7**, 537812 (2020)
[50] J. Luo, Grain boundary segregation models for high-entropy alloys: Theoretical formulation and application to elucidate high-entropy grain boundaries, Journal of Applied Physics **135**(16), 165303 (2024)
[51] B. Yin, W.A. Curtin, Origin of high strength in the CoCrFeNiPd high-entropy alloy, Materials Research Letters **8**(6), 209-215 (2020)

[52] P.-H. Ko, Y.-J. Lee, S.-Y. Chang, Microstructure and Mechanical Properties of Intergranular Boride Precipitation-Toughened HfMoNbTaTiZr Refractory High-Entropy Alloy, Materials **15**(19), 6666 (2022)
[53] X. Wang, M. Sun, J. Liu, X. Liu, W. Jiang, X. Wang, Q. Fang, The Microstructural Evolution and Mechanical Properties of Boron-Doped Ti35Zr30V10Nb25 Refractory High-Entropy Alloy, Crystals **14**(12), 1029 (2024)
[54] B. Kang, T. Kong, N.H. Dan, D.D. Phuong, H.J. Ryu, S.H. Hong, Effect of boron addition on the microstructure and mechanical properties of refractory Al0.1CrNbVMo high-entropy alloy, International Journal of Refractory Metals and Hard Materials **100**, 105636 (2021)
[55] P.-H. Ko, Y.-J. Lee, J.-H. Wang, C.-Y. Tsai, S.-Y. Chang, Boron interstitials strengthening grain boundary for toughening HfxMo0.5NbTaxTiV1.5-xZrx refractory high-entropy alloys, Materials Science and Engineering: A **923**, 147694 (2025)
[56] S.S. Nene, K. Liu, M. Frank, R.S. Mishra, R.E. Brennan, K.C. Cho, Z. Li, D. Raabe, Enhanced strength and ductility in a friction stir processing engineered dual phase high entropy alloy, Scientific Reports **7**(1), 16167 (2017)
[57] J.S. Song, B.J. Lee, W.J. Moon, S.I. Hong, Mechanical Performance and Microstructural Evolution of (NiCo)75Cr17Fe8Cx (x = 0~0.83) Medium Entropy Alloys at Room and Cryogenic Temperatures, Metals **10**(12), 1646 (2020)
[58] S. Tao, W. Jiang, W. Zhang, H. Qiu, S. Wu, S. Guo, B. Zhu, Microstructure evolution and mechanical properties of NbHfTiVCx novel refractory high entropy alloys with variable carbon content, Journal of Alloys and Compounds **928**, 166986 (2022)
[59] J. Wang, R. Janisch, G.K.H. Madsen, R. Drautz, First-principles study of carbon segregation in bcc iron symmetrical tilt grain boundaries, Acta Materialia **115**, 259-268 (2016)
[60] C. Zhang, C. Chen, L. Jiang, Y. Li, Z. Zhu, F. Chen, Z. Cao, W. Zhang, Effects of Interstitial Oxygen Content on Microstructures and Mechanical Properties of TiZrNb Refractory Medium-Entropy Alloy, Metals **15**(3), 250 (2025)
[61] E.G. Wagenhuber, V. Trindade, U. Krupp, The role of oxygen-grain-boundary diffusion during intercrystalline oxidation and intergranular fatigue crack propagation in alloy 718, Proc. Int. Symp. Superalloys Var. Deriv. Pittsburgh, PA, 2005, pp. 591-600

[62] H.L. Yao, Y.X. Yu, J.B. Sha, Microstructural evolution at grain boundary and deformation mechanism of Nb0.5TiZrV0.5 refractory high entropy alloy doped with Ce at room temperature, Journal of Materials Science & Technology **196**, 25-39 (2024)
[63] Q. Xu, D.-Z. Chen, C.-R. Wang, W.-C. Cao, Q. Wang, H.-Z. Cui, S.-Y. Zhang, R.-R. Chen, Effects of La on microstructure and mechanical properties of NbMoTiVSi0.2 refractory high entropy alloys, Transactions of Nonferrous Metals Society of China **31**(2), 512-520 (2021)
[64] A. Sundar, D.B. Ferron, Y.-J. Hu, L. Qi, Automated hierarchical screening of refractory multicomponent alloys with high intrinsic ductility and surface passivation potency, MRS Communications **12**(6), 1086-1095 (2022)
[65] C. Tandoc, Y.-J. Hu, L. Qi, P.K. Liaw, Mining of lattice distortion, strength, and intrinsic ductility of refractory high entropy alloys, npj Computational Materials **9**(1), 53 (2023)